Cohesive properties of refractory castable at 600°C: Effect of sintering and testing temperature

R Vargas, R B Canto, François Hild

Cohesive properties of refractory castable at 600°C: Effect of sintering and testing temperature

R. Vargas[a,c], R.B. Canto[a,b] and F. Hild[c]

[a] *Federal University of São Carlos, Graduate Program in Materials Science and Engineering (PPGCEM), 13565-905, São Carlos-SP, Brazil*
[b] *Federal University of São Carlos (UFSCar), Department of Materials Engineering (DEMa), 13565-905, São Carlos-SP, Brazil, Brazil*
[c] *Université Paris-Saclay, CentraleSupélec, ENS Paris-Saclay, CNRS, LMPS – Laboratoire de Mécanique Paris-Saclay, 91190 Gif-sur-Yvette, France*

ARTICLE INFO

Keywords:
Cohesive Zone Model (CZM)
Digital Image correlation (DIC)
Finite Element Model Updating (FEMU)
Refractory castable
Wedge Splitting Test (WST)

ABSTRACT

This paper aims to evaluate cohesive properties for an alumina refractory with mullite-zirconia aggregates from wedge splitting tests (WST), and to assess their sensitivity to sintering and testing temperature. Five experiments were analyzed of which four were performed at 600°C. The sought parameters were determined via weighted finite element model updating. The cohesive strength and the fracture energy were successfully calibrated and resulted in simulated data close to their experimental counterparts (*i.e.,* between 4 and 11 times the measurement uncertainty). Increasing the sintering temperature from 1400°C to 1450°C enhanced the cohesion between the mullite-zirconia aggregates and the alumina matrix (20% increase of the fracture energy and of the fracture process zone length). When the WSTs were performed at 600°C, the cohesive strength was 10% smaller while the fracture energy was 70% higher than that at room temperature.

1. Introduction

Material parameters are no more than measurements after external stimuli that lead to insight into the underlying medium. For instance, in a simplified manner, the mechanical strength is related to atomic forces, as the thermal expansion coefficient is an indirect measurement of how the stable bond radii change with temperature [1]. Moreover, these parameters are commonly used to make project decisions, recently being coupled with numerical simulations to better predict in-service reliability. Therefore, the success in the project is directly related to the knowledge of the parameters, which should be as representative as possible of in-service conditions [2] as they may considerably change with temperature variations or other external variables.

The present paper deals with refractories that are commonly utilized in hazardous applications involving high-temperature and/or corrosive environments [3]. In such conditions, it is crucial that they maintain functional properties to diminish risks. Moreover, predicting their durability helps to better schedule maintenance, thereby maximizing productivity while minimizing costs and waste of materials and energy. Even if functional properties are maintained, the presence of cracks is unavoidable in many cases due to critical thermomechanical loadings. One possible way to

*Corresponding author
r.vargas_m@ppgcem.ufscar.br (R. Vargas)
ORCID(s): 0000-0002-5524-1886 (R. Vargas); 0000-0002-9286-9912 (R.B. Canto); 0000-0001-5553-0066 (F. Hild)

analyze such phenomena is using Cohesive Zone Models (CZMs) [4, 5, 6, 7, 8] in which the whole fracture process is described in few elements of finite element models. Hereafter, cohesive parameters related to crack initiation and propagation will be calibrated for a refractory castable.

Although cohesive parameters can be used to simulate cracks, few studies discuss how to calibrate them at high temperatures. Mathias and Tessier-Doyen [9] used cohesive elements to describe the interface of a model material in which the inclusions shrank more than the matrix, thereby leading to debonding. However, the authors did not give details on the optimization procedure that was used to obtain the cohesive parameters. Özdemir et al. [10] used CZMs to describe interface debonding for thermal shocks with gradients in alumina-mullite samples. An inverse procedure was used to best fit the experimental results. Hein et al. [11] studied damage in a layered alumina and magnesia refractory under thermal shock using a CZM. The parameters were "*chosen without experimental exploration on real ceramics*" and changed to check their influence. Last, Doitrand et al. [12] calibrated a CZM with force and crack length data from Wedge Splitting Tests (WSTs) at room and elevated temperatures on a refractory ceramic. It is worth noting that from the previously discussed papers, this is the only reference that studied crack propagation at high-temperature. The authors showed how CZM parameters considerably changed when calibrated at 25°C, 800°C and 1200°C. It is worth noting that, to the authors' best knowledge, this is the only paper analyzing high-temperature WSTs using Digital Image correlation (DIC) coupled to CZM.

Earlier investigations also discussed the WST setup for high-temperature experiments. Harmuth et al. [13] presented results for WSTs performed at 1000°C, and their dependence on the loading rate for a magnesia-chromite material and up to 1500°C for several materials to provide guidelines for product development [14]. Buchebner et al. [15] used WSTs up to 1500°C to improve material selection and product development, while Brisson et al. [16] performed them at 1200°C and 1400°C to check the effect of andalusite grain size on microstructure and mechanical properties. Brochen et al. [17] also performed WSTs at 1400°C to estimate the fracture energy of magnesia-carbon samples in argon atmosphere to mitigate oxidation. Andreev et al. [18] compared different testing methodologies, including WSTs at room-temperature, 800°C, and 1100°C to assess thermal shock properties in silica refractories. Jin and Harmuth [19] used WSTs from 900°C to 1500°C to calibrate parameters for an asymmetric creep model for magnesia chromite. Similarly, Samadi et al. [20] used 1200°C WSTs to calibrate damage and creep parameters of alumina spinel.

The five experiments analyzed herein were introduced in Ref. [21]. The challenges of not having the full field of view led to the study of Notch Opening Displacement (NOD) vs. Crack Mouth Opening Displacement (CMOD) relationship [22], which was then applied and validated to calibrate CZM parameters for room temperature experiments [23]. The present paper proposes to apply this methodology for 600°C experiments, discussing the necessary adjustments to obtain further insight into the effect of different heat treatments and testing conditions. First, the ma-

terial and experiments are introduced. The identification framework is then discussed, highlighting the FE model, the chosen parameters and how to initialize them, together with the needed filtering due to noisier DIC measurements at higher temperature. Last, the five experiments are discussed in terms of cohesive strength, fracture energy, and fracture process zone size related to the firing temperature and testing conditions.

2. Material and Methods

This section first discusses the studied material. Then, the so-called wedge splitting test is introduced together with the five experiments analyzed herein.

2.1. Studied castable

The refractory castable used herein was the SUPERCASTIBAR 85 MZ grade produced by IBAR (Indústria Brasileira de Artigos Refratários, Poá-Brazil). It had a low cement content and was composed of an alumina matrix (maximum aggregate size: 3.3 mm) together with smaller mullite-zirconia particles whose diameter ranged from 0.5 mm to 2.5 mm. The typical oxides included Al_2O_3 (86%wt), ZrO_2 (8 wt%), SiO_2 (4 wt%), CaO (1.8 wt%), and Fe_2O_3 (0.1 wt%). Consequently, little to no liquid phase was expected to occur during sintering below 1500°C. This composition was chosen due to its industrial relevance together with the presence of zirconia that brings interesting attributes for developing methodologies (*i.e.,* martensitic phase transformation between 950°C and 1150°C [24], toughening mechanisms [25, 26], as well as suitable contrast for tomographic analyzes [27]).

For the present study, the main question is related to the cohesive parameters and their variation with sample preparation (*e.g.,* firing temperature of the sample and/or the presence of lateral grooves to guide the crack propagation) and with the testing temperature. The samples were cast from the same lot of mixture provided by IBAR, after adding 5.2 wt% of water and homogenization. Three batches were required since only two molds were available. The molds were similar to those utilized in Ref. [28], with a small change in the angle of the surfaces where the splitting force was applied [22]. The samples were cured for 24 h at room temperature with 80% humidity, and then dried at 110°C for another 24 h. A pre-fire of 5 h at 600°C after heating up at a rate of 1°C/min was performed before getting back to room temperature. Two firing temperatures were investigated, namely, 1400°C and 1450°C, with a heating rate of 3°C/min up to 600°C followed by 1°C/min until the final temperature where the treatment lasted 5 h. Therefore, the microstructure was fully consolidated at the testing temperature of 600°C. The 3D renderings of an internal region of post-mortem tomographic volumes for samples MZ2-1400 (Figure 1(a)) and MZ4-1450 (Figure 1(b)) show that the grains and porosity distributions were similar for the two different heat treatments studied herein (see nomenclature in the following section).

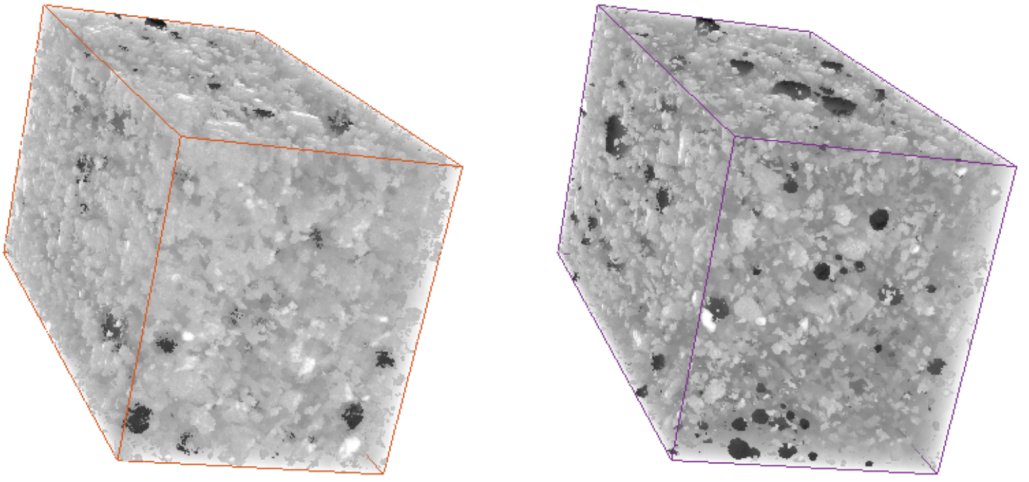

(a) (b)

Figure 1: 3D rendering of $\approx 29 \times 25 \times 52$ mm^3 tomographic volumes of samples MZ2-S1400 (a) and MZ4-S1450 (b).

One representative view of the microstructure is shown in Figure 2. No polishing was performed prior to image acquisition to highlight the topography of the aggregates. Figure 2(a) shows two adjacent mullite-zirconia aggregates. One aggregate exhibited a eutectic microstructure (Figure 2(b)) while white and rounded primary zirconia formations are seen on another one (Figure 2(c)), indicating local higher zirconia composition [29]. A third aggregate from a different region is shown in Figure 2(d) with both eutectic dendrites together with primary zirconia. The use of fused mullite-zirconia aggregates with eutectic microstructures was compared to a reference high-alumina composition [30, 31], and it was shown that it led to higher thermomechanical properties (*e.g.,* fracture energy), which was related to an increased volumetric crack density [30] and crack deflection inside the aggregates.

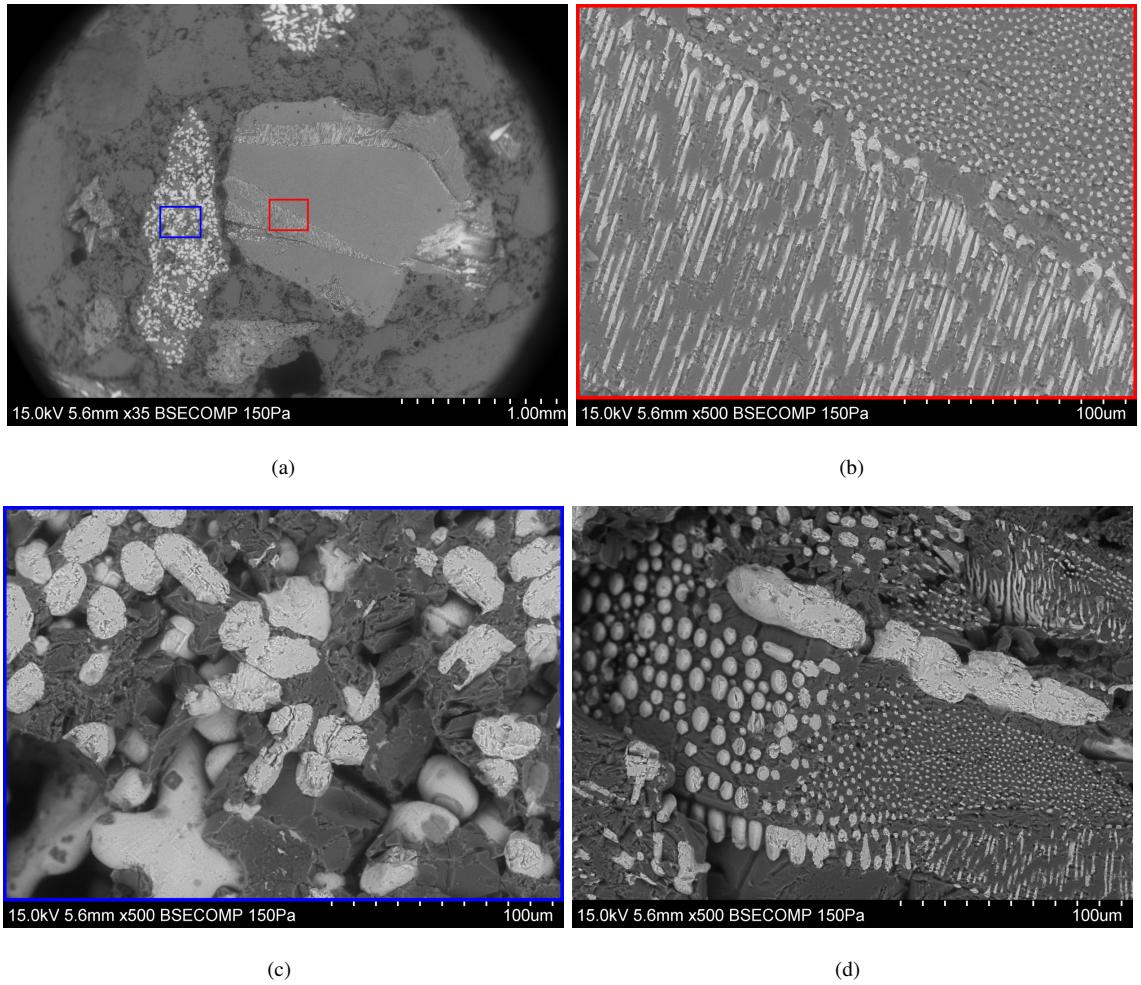

Figure 2: SEM images of the microstructure obtained in backscattered electron mode. Two adjacent mullite-zirconia aggregates (a), with eutectic dendrites (b), and rounded primary zirconia (c). Another aggregate is shown (d) with both structures seen in sub-figures (b) and (c).

2.2. Wedge splitting tests

Five WSTs are analyzed hereafter, namely, the same that were discussed in Refs. [21, 22, 23]. All the specimens were made with the same material described in the previous section, designated as "MZ". Two features were changed, which will be recalled in their designation. First, the sintering temperature, which is defined after an "S" (*i.e.,* it was either equal to 1400°C or 1450°C). Second, the presence of lateral grooves to guide crack propagation, which is indicated by the presence of a "G" in the nomenclature. Moreover, the samples are numbered sequentially for the sake of clarity. For example, the first specimen tested is MZ1-S1450G, meaning that it was sintered at 1450°C and had lateral grooves.

The first two specimens (*i.e.,* MZ1-S1450G and MZ2-S1400) were tested under monotonic loading history at

room temperature and 600°C, respectively (Figure 3). The chosen testing temperature was the highest possible with the present furnace and led to the understanding on how to treat the acquired images [32] before preparing the setup and performing such experiments at higher temperatures for which further challenges will arise such as black body radiations [33]. All the other experiments (*i.e.,* MZ3-S1400G, MZ4-S1450, and MZ5-S1450G) had five cycles and were performed at 600°C. However, only the load envelope up to 15% of the ultimate load was used in the discussion hereafter.

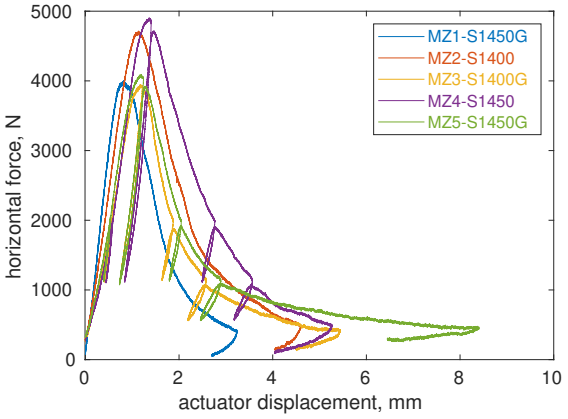

Figure 3: Full loading curves (*i.e.,* horizontal force vs. actuator displacement) for the five experiments analyzed herein. Apart from MZ1-S1450G (room temperature), all the other WSTs were performed at 600°C.

From the loading curves shown in Figure 3, it is concluded that the 1450°C firing led to slightly higher ultimate forces and dissipated energy in the post-peak regime than the samples fired at 1400°C. It is worth noting that the curve from MZ1-S1450G (performed at room-temperature) cannot be directly compared to the other ones (*i.e.,* the flexibility of setup changes with temperature). Although its initial slope is higher than the other cases, the NOD vs. horizontal force curves reported in Ref. [21] had similar initial slopes for every case irrespective of the testing temperature. This point highlights that displacement measurements should be made on the sample whenever possible to mitigate differences related to the setup and not the material.

3. Calibration procedure of CZM parameters

This part deals with the calibration of CZM parameters for four experiments performed at 600°C using measured NODs to drive FE simulations. The Finite Element (FE) model is first introduced, highlighting the geometry, boundary conditions and all the parameters of interest. Second, the need for filtering the NODs measured at 600°C is discussed, since the uncertainty was one order of magnitude higher in comparison to room temperature experiments. Last, the so-called Finite Element Model Updating (or FEMU [34, 35, 36]) framework is introduced.

3.1. Finite Element model

All the necessary features for defining the FE model are summarized in Figure 4. A first mesh was built as shown in Figure 4(a) based on the sample geometry [22]. In the present setup, the loading region was not visible in the pictures (see field of view in orange dashed box in Figure 4(a)). Then this mesh was scaled and positioned in the image frame so that the NOD regions (cyan squares) coincided with the measurement zones via DIC [21]. The NOD was then extrapolated to CMOD data [23] as described in the following sections, and applied on two nodes in the force application region (green circles). Quadrilateral elements (Figure 4(b)) were used to define a different section with reduced thickness for the samples that had lateral grooves to guide the crack.

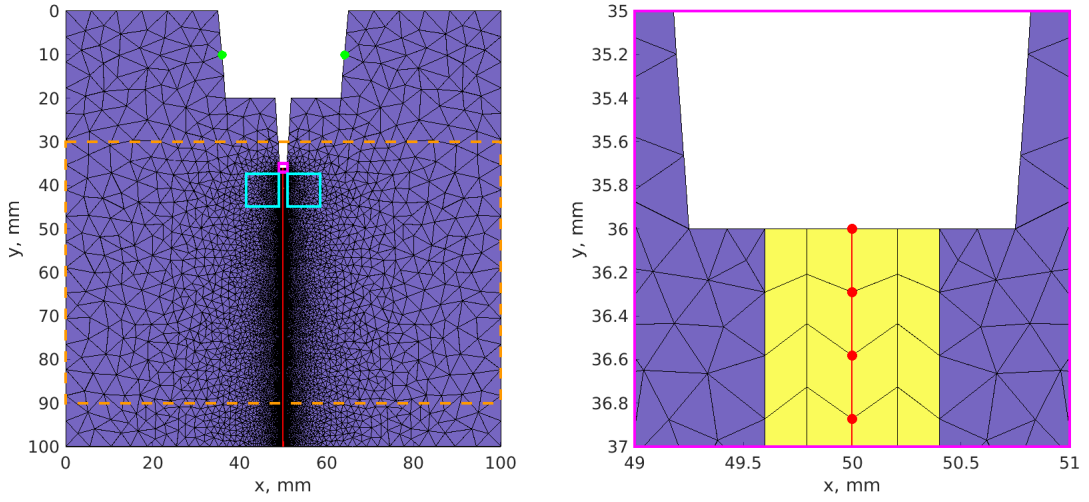

(a) (b)

Figure 4: (a) Mesh for the finite elements analyses. The NOD region is depicted as cyan squares, and the two nodes where the boundary conditions were applied as green circles. One line of zero thickness cohesive elements was used in the crack propagation region and is shown as a red line. The available field of view is depicted as a dashed orange box. (b) Zoom about the pre-notch. CPE3 elements are shown in blue and CPE4 elements in yellow. The red circles highlight the duplicated nodes used in the PPR cohesive elements.

Zero-thickness cohesive elements were used in the ligament (Figure 4) defined with the so-called PPR cohesive model [8, 37]. Since this experiment could be considered as a pure mode I loading, no sensitivity was expected to calibrate the parameters for mode II crack propagation. Therefore, they were considered to be equal to the mode I parameters for the sake of simplicity. The initial slope parameter was kept constant and equal to 0.005 [38]. Two values for the shape parameters, α, were investigated. Their influence is shown in Figure 5. When $\alpha = 2$, the damage law is bi-linear. For $\alpha = 7$, an exponential decay is observed. Both traction-separation curves correspond to the same

initial fracture parameters, namely, σ_f, the cohesive strength and J_c, the fracture energy (Table 1). Thus, even though the overall shape is different, the peak stress and the curve integrals are strictly identical in the present illustration. Both parameters σ_{max} and J_c were calibrated in the identification procedure.

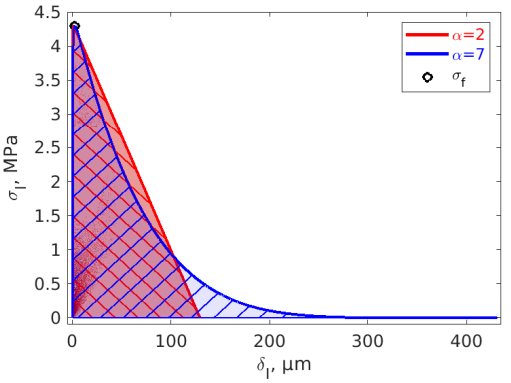

Figure 5: Mode I traction-separation law using the initial parameters of the PPR model (Table 1). The cohesive strength σ_f corresponds to the maximum traction (black circle), and the fracture energy J_c is the integral of the traction-separation curve (dashed areas).

Three more parameters, which are related to the boundary conditions, were needed together with the two cohesive parameters to fully define the calibration step. The Boundary Condition correction (BCc) gives an offset related to the non-zero load at the reference image and possible misalignment of the wedge [38]. It is defined as a scalar subtracted by one that multiplies the boundary conditions at the point where the load is half the peak load. A value of $BCc = 1$ means that no correction was needed. For instance, $BCc = 1.2$ means that 20% of the boundary condition for the point at 50% of the peak load was required to correct the initial state. Moreover, a BCc level less than one signifies that a compressive correction was needed.

The last two parameters are the ratio between the CMOD (Δ) and NOD (δ) at the peak load, R and the slope of the CMOD vs. NOD curve post-peak, c, after the observations and proposal from Ref. [23]. They need to be calibrated since the present setup did not allow for DIC measurements in the CMOD region. The CMOD that is used as the applied boundary condition is expressed as

$$\bar{\delta} = \left(\frac{R}{c} - 1\right)\bar{\Delta}^2 + \left(2 - \frac{R}{c}\right)\bar{\Delta} \tag{1}$$

for the pre-peak regime and

$$\bar{\delta} - 1 = \frac{R}{c}\left(\bar{\Delta} - 1\right) \tag{2}$$

for the post-peak regime [22], where $\bar{\delta}$ and $\bar{\Delta}$ are the NOD and CMOD normalized by their respective values at the peak load. Although the Young's modulus was calibrated in Ref. [23] for room-temperature experiments (with rather

low sensitivities), the higher uncertainty for the 600°C tests led to unrealistic levels. Therefore, the Young's modulus was kept constant and equal to 46 GPa, which was identified for the first experiment discussed in Section 4. All the initial parameters are gathered in Table 1, as calibrated in Ref. [23] with the same identification framework.

Table 1

Initial parameters for the presented analyses

Parameter	Description	MZ material
σ_f [MPa]	Cohesive strength	4.3
J_c [J/m^2]	Fracture energy	280
R	NOD vs. CMOD ratio at ultimate load	2.2
c	Slope for the post-peak NOD vs. CMOD affine trend	1.5
BCc	Boundary condition correction	1

3.2. Temporal interpolation of NOD measurements

The identification methodology used herein was introduced in Ref. [23] using room temperature tests. However, the uncertainties for the images acquired for the WSTs performed at 600°C were one order of magnitude higher [21]. Therefore, the raw measurements were very noisy and led to large oscillations if used directly as boundary conditions in the identification scheme. Filtering the high frequency oscillations in NOD data before extrapolating them to CMODs, the so-called cubic Hermite splines were used [39]. They consist of four cubic functions, tailored in a way that the degrees of freedom represent the value and first derivative of the function at both ends of any given interval. To capture the curvature details of the experimentally measured NODs, nine intervals were chosen. Twelve equally spaced points were defined, and then the second and eleventh were removed. With this setting, the first and last intervals are twice the size of the others. The continuity of the interpolation function and its first derivatives was thus enforced over the whole temporal domain. With such hypotheses, only twenty degrees of freedom were needed. They were obtained through least squares minimization between the raw measurements and the selected interpolation function.

Figure 6 illustrates such filtering using the first high-temperature case (*i.e.,* test MZ2-S1400) as an example. The loading curve is first shown, in which the 10 points of interest are highlighted with vertical dashed lines. Second, the 9 Hermite splines used in the present approach are represented. Last, the experimental and filtered NODs are shown. The standard deviation of their differences was equal to 1.6 times the corresponding measurement uncertainty, which is very low. For the five tests investigated herein, the standard deviation was always less than twice the standard measurement uncertainty, which validated the proposed interpolation.

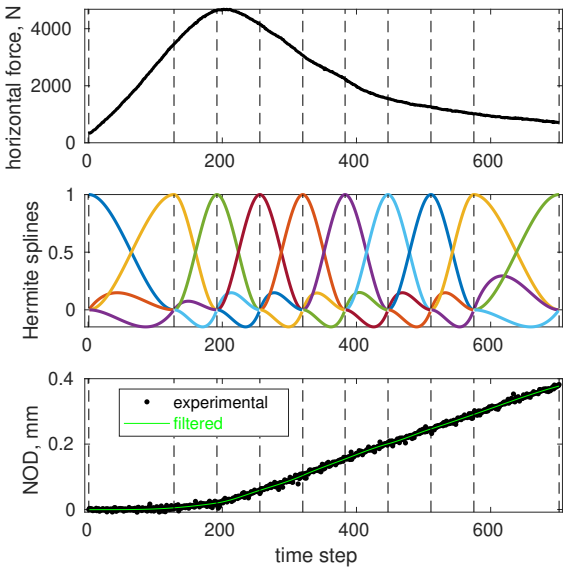

Figure 6: Experimental horizontal force (test MZ2-S1400), Hermite splines, experimental and filtered NODs as functions of time steps. The vertical dashed lines depict the ten points of interest used to define the splines.

3.3. Identification strategy

The FEMU method was used to calibrate the CZM and boundary condition parameters discussed in Section 3.1. Two measured quantities were used in the global cost function, namely, the force (acquired by the load cell) and the NOD data (measured via DIC and filtered). These quantities are depending on n_p parameters, which are gathered in the column vector $\{\mathbf{p}\}$. Therefore, two cost functions are written, χ^2_F giving the error in the horizontal (splitting) force of the experiments

$$\chi^2_F(\{\mathbf{p}\}) = \frac{1}{n_t}\sum_t \left(\frac{F_m(t) - F_{\mathrm{FE}}(t,\{\mathbf{p}\})}{\gamma_F}\right)^2 \tag{3}$$

and χ^2_{NOD} that characterizes the difference between measured and simulated NODs

$$\chi^2_{\mathrm{NOD}}(\{\mathbf{p}\}) = \frac{1}{n_t}\sum_t \left(\frac{\mathrm{NOD}_m(t) - \mathrm{NOD}_{\mathrm{FE}}(t,\{\mathbf{p}\})}{\gamma_{\mathrm{NOD}}}\right)^2 \tag{4}$$

where n_t is the number of time steps, the subscript m is related to measured and FE to computed quantities. Both cost functions are normalized by the corresponding standard measurement uncertainties (*i.e.,* γ_F and γ_{NOD}), so that the χ values become dimensionless and represent how many times the uncertainty this error represents, a direct measurement of the quality of the identification. A value of $\chi = 1$ is then the lower bound that indicates that the error can be fully explained by the experimental measurements. Therefore, the closest χ is to unity, the better the simulation represents the experiment.

Both χ_F and χ_{NOD} are combined in a single cost function, χ_{tot} considering the same weights from Bayesian

statistics [40]

$$\chi^2_{tot}(\{\mathbf{p}\}) = \frac{1}{2}\chi^2_F(\{\mathbf{p}\}) + \frac{1}{2}\chi^2_{\mathrm{NOD}}(\{\mathbf{p}\}) \tag{5}$$

since a single point for each quantity is present for each time step. The cost function χ_{tot} is minimized via nonlinear least squares minimization, based on a Gauss-Newton scheme in the same framework introduced in Ref. [23]. The interested reader is referred to the previous paper and to Appendix A where more information is given about the identification scheme.

4. Analyses of the five tests

This section gathers all identification results from the five analyzed tests. First, the force and NOD curves for the converged procedure are shown for each case. They are all presented until 15% of the peak load. The last three tests were cyclic, but only the envelope was kept. The cost functions (*i.e.,* χ_F and χ_{NOD}) are reported in Table 3, and the calibrated parameters for all experiments in Table 11 for $\alpha = 2$, as well as Tables 4 and 5 for $\alpha = 7$.

4.1. Measurement uncertainties

In the proposed identification framework, the standard measurement uncertainties (*i.e.,* γ_F and γ_{NOD}) are needed. For the load uncertainty, the forces were recorded during the acquisition of the 100 reference images for each analyzed case, and their standard deviation γ_F was equal to 10 N for the splitting force. Since similar levels were observed in all experiments, the same value γ_F was used. This evaluation of γ_F corresponds to the noise floor level. Another possibility is to use the NOD uncertainty to quantify the force oscillations in the simulations due to the fact that they were driven by measured displacements [41]. Such approach was not performed herein.

For the NOD uncertainty, the initial 100 reference images (for each experiment) were analyzed and the respective values are shown in Table 2. The standard uncertainty $\gamma_{NOD} = 0.2$ µm for the room temperature test (*i.e.,* 2×10^{-2} px or 2 cpx) is typical of standard DIC conditions [42]. For the 600°C tests, all uncertainties were one order of magnitude higher, ranging from 2.7 to 3.3 µm, depending on the sample texture. This points reinforces the importance of quantifying the uncertainties, and how heat haze affected the acquired images during such experiments [21].

Table 2

Standard measurement uncertainties for all five analyzed tests

Uncertainty	MZ1-S1450G	MZ2-S1400	MZ3-S1400G	MZ4-S1450	MZ5-S1450G
γ_{F} [N]	10	10	10	10	10
γ_{NOD} [µm]	0.2	2.8	3.1	2.7	3.3

4.2. Room temperature test

The results for test MZ1-S1450G, the only experiment performed at room temperature, is shown in Figure 7 in which the splitting force and NOD data are reported as functions of the actuator displacement. The experimental data are compared to the predictions of the calibrated PPR law for the two investigated values of α. All the calibrated parameters are reported in Tables 4, 5, and 11. The calibration results for this test using $\alpha = 7$ and more time steps (from 15% to 10% of the peak load) were reported in Ref. [23]. The benefits of using $\alpha = 7$ instead of $\alpha = 2$ is visible in the load vs. actuator displacement curve (Figure 7(a)), with a χ_F reduction from 14.7 to 6.6, but not on the NOD data (Figure 7(b)), where χ_{NOD} varied from 3.3 to 3.8. The three reported NOD curves are almost superimposed with very small differences.

If same weight is given to force and NOD data, as chosen herein, the total residual χ_{tot} indicates that using $\alpha = 7$ is better than $\alpha = 2$ for this case (*i.e.,* χ_{tot} was equal to 5.2 with $\alpha = 7$ in comparison to 9.0 for $\alpha = 2$). Both CZM parameters were higher when $\alpha = 7$ was used, *i.e.,* $\sigma_f = 4.3$ MPa and $J_c = 266$ J/m^2, instead of $\sigma_f = 4.0$ MPa and $J_c = 249$ J/m^2 for $\alpha = 2$. Moreover, all the other parameters related to the boundary conditions (*i.e.,* R, c, and BCc) presented less than 5% differences. Another direct comparison is with the identification performed in Ref. [23] that used the same experiment with $\alpha = 7$ but with more time steps in the end of the test. If all the image set was used, $\chi_{tot} = 6.2$, namely, higher than the level found herein. Overall, the obtained parameters were very similar (*e.g.,* with a difference around 1% for σ_f). The biggest change came from the fracture energy $J_c = 283$ J/m^2 (*i.e.,* 6% higher). This observation highlights how difficult it is to describe advanced stages of crack propagation and that J_c is the most influenced parameter when more time steps were added at the very end of the propagation step.

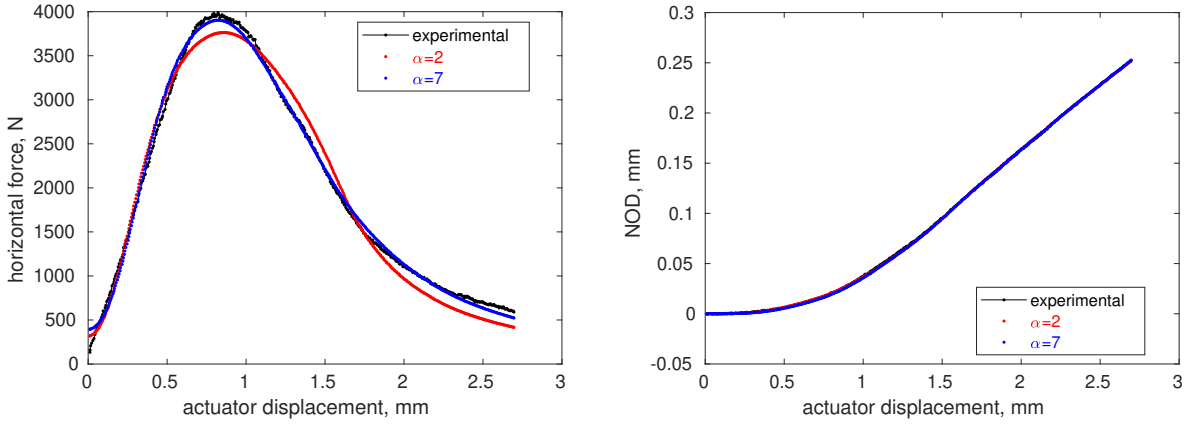

(a) (b)

Figure 7: Experimental and simulated force (a) and NOD (b) vs. actuator displacement for test MZ1-S1450G.

4.3. High temperature tests (600°C) on 1400°C fired castable

The results for sample MZ2-S1400, which was the first test performed at 600°C, are shown in Figure 8. It is worth noting that only this sample and MZ4-S1450 had no lateral grooves to guide the crack, which means that even smaller displacements are expected in the pre-loading step due to smaller sample flexibility. The overall loading curve is well captured in both cases, with $\alpha = 7$ giving the best result (*i.e.,* $\chi_F = 13.4$ instead of $\chi_F = 20.5$). Although the experimental NOD was significantly noisier than for the previous case, both values of α captured the overall tendencies, with differences at the end of the test and near the peak load. In terms of NODs, low levels of χ_{NOD} were achieved (*i.e.,* 2.1 and 1.9 for α equal to 2 and 7, respectively). The total residual χ_{tot} indicates that $\alpha = 7$ was to be preferred, since a value of 7.6 was obtained (in comparison to 11.3). For the CZM parameters, $\alpha = 2$ yielded a cohesive strength $\sigma_f = 3.2$ MPa and a fracture energy $J_c = 316$ J/m^2, which increased to 3.5 MPa and 327 J/m^2 when α was changed to 7. For the NOD parameters, the coefficients R and c reduced slightly. The boundary condition parameter BCc increased by less than 5%.

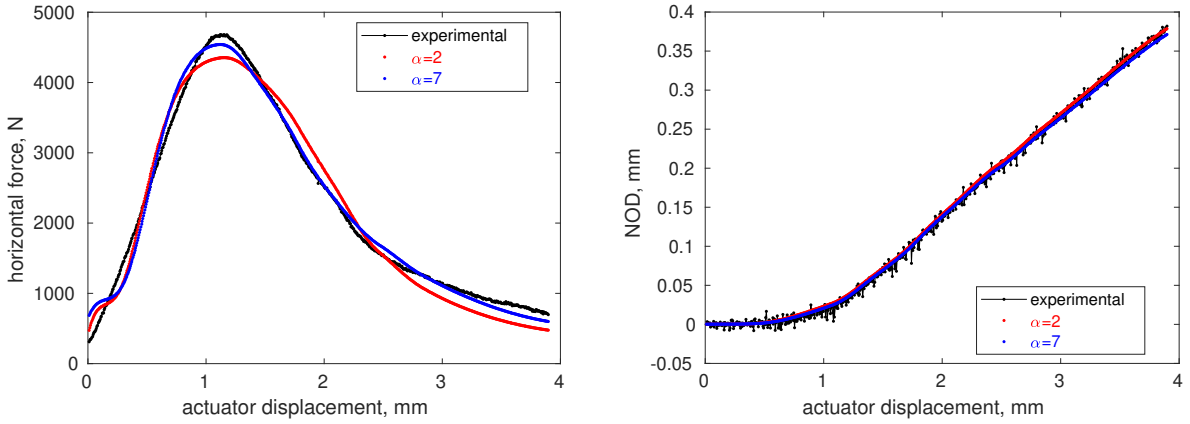

(a) (b)

Figure 8: Experimental and simulated force (a) and NOD (b) vs. actuator displacement for test MZ2-S1400.

The last three experiments had five cycles, but only the envelope is shown, which explains the small discontinuities in the experimental curves. Results for sample MZ3-S1400G are shown in Figure 9. Both values of α capture the overall trends of the horizontal force history. Although they deviate in some regions from the experimental data, the case $\alpha = 7$ shows a better agreement with $\chi_F = 14.7$ in comparison to $\chi_F = 25$ when $\alpha = 2$. One possible cause for this deviation was that the cycles were not accounted for. For the NODs, no difference is visible for both simulations with very similar χ_{NOD} levels (*i.e.,* 4.2 and 4.5), and both cases deviate from the experimental curve especially around 1 mm of actuator displacement (*i.e.,* near the peak load). Just changing α from 2 to 7, reduced χ_{tot} from 14.6 to 9.6, which is significant. A difference of almost 10% is observed in the CZM parameters, with the cohesive strength σ_f

increasing from 3.5 to 3.9 MPa, and the fracture energy J_c from 338 to 361 J/m^2. The other parameters remained close, with the coefficient R being the one that changed the most, from 1.50 to 1.41.

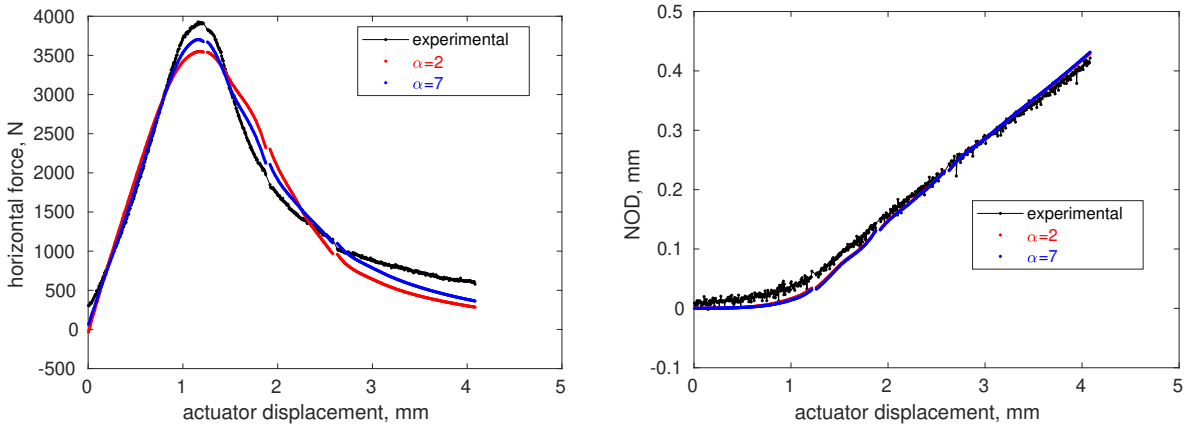

(a) (b)

Figure 9: Experimental and simulated force (a) and NOD (b) vs. actuator displacement for test MZ3-S1400G.

4.4. High temperature tests (600°C) on 1450° fired castable

The results for test MZ4-S1450, namely, the second sample with no lateral groove, are presented in Figure 10. The value $\alpha = 2$ captures the overall curvature of the loading curve, but using $\alpha = 7$ led to the best agreement with respect to the experimental curve among the five analyzed tests (*i.e.,* smallest χ_F, decreasing from 19.2 to 5.9). The three NOD curves are very similar, and again no visual difference are distinguished with a $\chi_{NOD} = 2.5$ and 2.6, respectively. Since χ_{NOD} is almost identical, $\alpha = 7$ should be selected since it led to a lower $\chi_{tot} = 4.2$ (*i.e.,* less than 10.9 for the other value). Similar to the previous cases, both CZM parameters were between 5% to 10% higher when $\alpha = 7$ was used (*i.e.,* σ_f increases from 3.3 MPa to 3.7 MPa and J_c from 383 J/m^2 to 404 J/m^2). The parameters R and BCc were slightly higher (1.59 instead of 1.68, and 1.22 instead of 1.19, respectively), while c remained almost constant around 1.53.

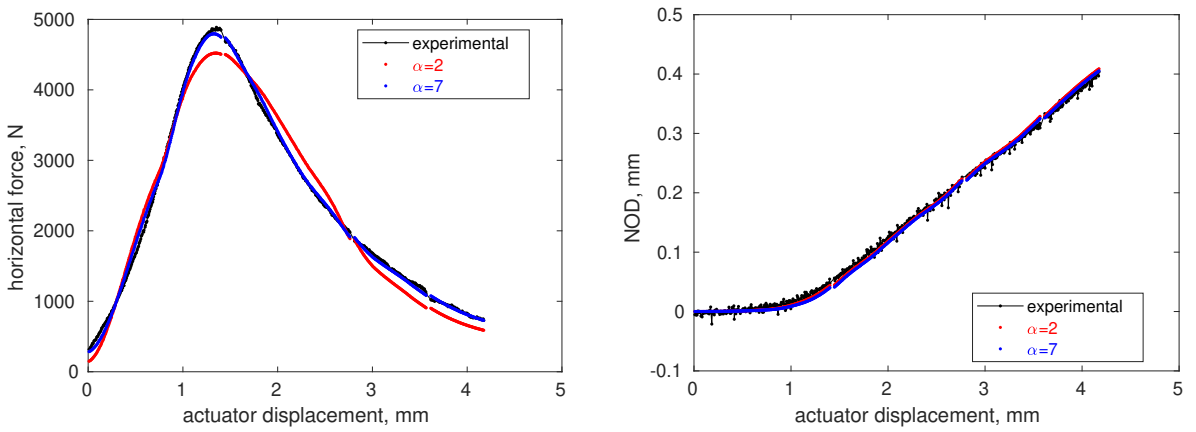

(a) (b)

Figure 10: Experimental and simulated force (a) and NOD (b) vs. actuator displacement for test MZ4-S1450.

The analysis of the fifth experiment, using sample MZ5-S1450G, is displayed in Figure 11. The overall trend is similar to what was discussed for test MZ3-S1400G, in which both simulations deviate in certain regions from the experimental data, with some improvements observed with $\alpha = 7$ for which $\chi_F = 19.8$ in contrast to $\chi_F = 29.6$ when $\alpha = 2$. The best NOD report (*i.e.,* lowest χ_{NOD}) among the five studied experiments was found for this case, with a smallest χ_{NOD} of 1.5 and 1.7 for $\alpha = 2$ and 7, respectively. Even if χ_{NOD} was slightly lower using $\alpha = 2$, the total residual χ_{tot} was equal to 15.6, greater than $\chi_{tot} = 10.7$ obtained with $\alpha = 7$. The same observation as in previous cases is seen here for the CZM parameters being 5 to 10% higher when $\alpha = 7$ (*i.e.,* $\sigma_f = 3.8$ MPa and $J_c = 456$ J/m^2 in comparison to 3.5 MPa and 422 J/m^2). Among the other parameters, using $\alpha = 7$ only the R parameter was smaller (1.68 instead of 1.76), while c remained quasi constant (1.51 and 1.49) and BCc increased a bit (1.69 and 1.67).

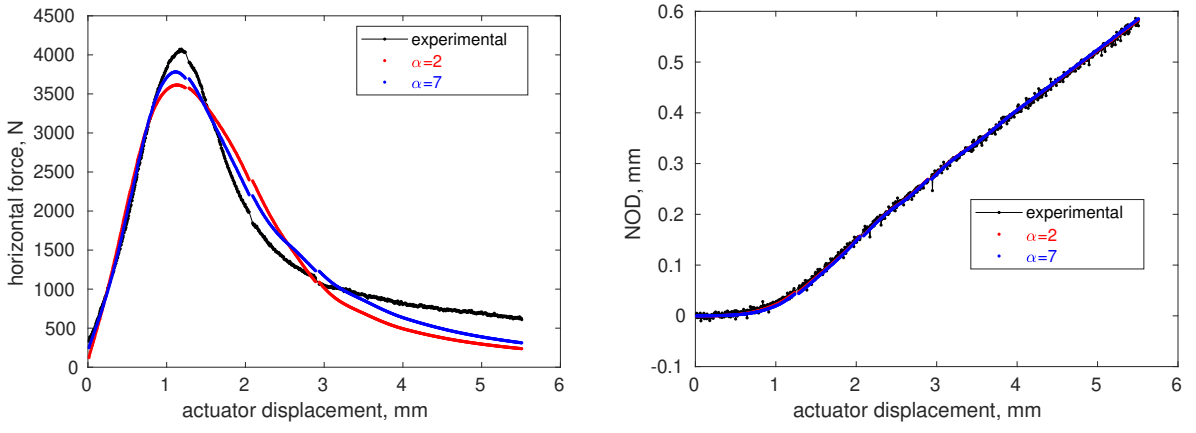

(a) (b)

Figure 11: Experimental and simulated force (a) and NOD (b) vs. actuator displacement for test MZ5-S1450G.

5. Discussion

5.1. Choice of the shape parameter α

As illustrated in Section 3.1, the shape of the traction-separation law is defined by the parameter α (Figure 5). All cost-functions are gathered in Table 3 for both $\alpha = 2$ and $\alpha = 7$. The levels of χ_{F} were all lower when using $\alpha = 7$. Only MZ2-1400 had a smaller χ_{NOD} when using $\alpha = 7$, although they changed less. The NOD data were very close to the experiments (*i.e.,* χ_{NOD} were very close to unity) in comparison to the load data (*i.e.,* χ_F was significantly higher). By coupling them, the identification procedure could successfully calibrate the parameters of interest in very few iterations. The consistently smaller χ_{tot} indicates that between the investigated values of α, $\alpha = 7$ was to be preferred in *all* five experiments. Therefore, the following results will only be discussed for $\alpha = 7$. The interested reader will find the calibrated parameters using $\alpha = 2$ in Table 11 of Appendix B. The levels of χ_{tot} were about ten times the measurement uncertainties, which are deemed to be low given the complexity of the experiments.

All These results indicate that the chosen PPR model accurately described the fracture phenomena by simplifying the toughening mechanisms with a traction-separation law that models the mechanical behavior with zero-thickness lines of cohesive elements.

Table 3

Cost functions for both studied CZM traction-separation law shapes

Cost function	MZ1-S1450G	MZ2-S1400	MZ3-S1400G	MZ4-S1450	MZ5-S1450G
$\chi_F(\alpha = 2)$	14.7	20.5	25.0	19.2	29.6
$\chi_F(\alpha = 7)$	6.6	13.4	14.7	5.9	19.8
$\chi_{NOD}(\alpha = 2)$	3.3	2.1	4.2	2.5	1.5
$\chi_{NOD}(\alpha = 7)$	3.8	1.9	4.5	2.6	1.7
$\chi_{tot}(\alpha = 2)$	9.0	11.3	14.6	10.9	15.6
$\chi_{tot}(\alpha = 7)$	5.2	7.6	9.6	4.2	10.7

5.2. Boundary condition parameters

All the parameters related to boundary conditions (*i.e.,* R, c, and BCc) calibrated using $\alpha = 7$ together with their standard uncertainty (calculated from the covariance matrix as explained in Appendix A) are reported in Table 4. It is worth noting that the variation between different samples was higher compared to the reported standard uncertainty. More samples would be needed for concluding on this point. The reported parameter uncertainties were very low in all cases since they were related to the noise floor levels reported in Table 2. Even though the high temperature tests presented about fifteen times higher noise levels (Table 2), the parameter uncertainties remained similar since the higher temperature tests had more time steps than experiment MZ1-S1450G that was performed at room temperature (*i.e.,*

on average 1.6 times more in comparison with 486, considering only the envelopes). No clear trends were observed for these parameters. The scatter of R is rather high, from 1.4 up to 2.4, which is related to alignment imperfections. The NOD parameter c varied less. From the present analyses only a range of variation may be given as guideline (*i.e.,* between 1.41 and 1.62). The BCc coefficient shows that the wedge may be misaligned at the beginning of the test, given the fact that it could be caused by some porosity or the presence of an aggregate that may initiate the crack on one of the specimen sides. This variation highlights the interest of having images from both sides of the sample, which was not possible in the present setup, and could help to better understand such scatter [43].

Table 4

Converged parameter sets related to boundary conditions for identifications using $\alpha = 7$ with respective standard uncertainties ($\pm$)

Parameter	MZ1-S1450G	MZ2-S1400	MZ3-S1400G	MZ4-S1450	MZ5-S1450G
R	2.262 ± 0.0009	2.364 ± 0.001	1.408 ± 0.0009	1.593 ± 0.0007	1.675 ± 0.0009
c	1.4522 ± 0.0002	1.414 ± 0.0008	1.614 ± 0.0009	1.528 ± 0.0008	1.507 ± 0.0005
BCc	1.216 ± 0.0009	2.191 ± 0.001	1.084 ± 0.0008	1.219 ± 0.0005	1.688 ± 0.0009

5.3. Material parameters

The parameters of the CZM (*i.e.,* σ_f and J_c) using $\alpha = 7$ are gathered in Table 5. All high-temperature cases led to lower cohesive strengths and higher fracture energies than the room temperature experiment. This trend may be explained by smaller energy bonds at higher temperature coupled with higher mismatch due to different thermal expansion coefficients [31] together with mullite-zirconia aggregates being weakly bonded to the alumina matrix at lower sintering temperatures [44]. By comparing MZ2-S1400 to MZ3-S1400G, and MZ4-S1450 to MZ5-S1450G tests, the effect of having lateral grooves to guide the crack can be assessed. When grooves were implemented, an increase of both cohesive parameters σ_f and J_c of about 10% was observed. Such observations are explained by the weakest link theory for brittle materials to initiate cracks together with the presence of toughening mechanisms during crack propagation. In the presence of grooves, the crack path was induced, and therefore it did not necessarily follow the weakest path [45], which would dissipate less energy in cases with grooves, as seen for the fracture energy estimated via NOD data [21]. However, an inversion is seen here, with the grooved cases leading to higher values of J_c. It is worth noting that the crack path was considered to be straight even for the cases with no groove. In Ref. [41], the hypothesis of a straight crack path in an experiment where the crack path was curved increased the CZM parameters, especially J_c (more than 10%), compensating for shorter crack path. Therefore, if curved crack paths were finely described in tests MZ2-S1400 and MZ4-S1450, it is envisioned that the difference in parameters would become even higher.

Table 5

Converged parameter sets for identifications using $\alpha = 7$ with respective standard uncertainties ($\pm$)

Parameter	MZ1-S1450G	MZ2-S1400	MZ3-S1400G	MZ4-S1450	MZ5-S1450G
σ_f [MPa]	4.337 $\pm$ 0.002	3.541 $\pm$ 0.001	3.853 $\pm$ 0.001	3.675 $\pm$ 0.001	3.803 $\pm$ 0.001
J_c [J/m^2]	265.5 $\pm$ 0.1	327.3 $\pm$ 0.2	360.9 $\pm$ 0.2	404.5 $\pm$ 0.2	455.8 $\pm$ 0.2

The effect of different sintering temperatures are investigated by comparing tests MZ2-S1400 to MZ4-S1450, and MZ3-S1400G to MZ5-S1450G. Both parameters σ_f and J_c increased by about 10%, the latter being slightly more influential. Increasing the sintering temperature may not change much the cohesive strength since the biggest defect for crack initiation remains the pre-notch (even more critical in the presence of lateral grooves). However, the material cohesion is stronger in the matrix and the interfaces, which may cause more interlocks and friction between aggregates during crack propagation, reflecting in higher fracture energies.

As above-discussed, an increase of the sintering temperature led to a significant rise of the fracture energy. The fractured surfaces of samples MZ3-S1400G and MZ5-S1450G were imaged in an SEM (backscattered electrons mode) to further investigate this phenomenon. One of the four detectors had its polarity inverted to improve the topographic perception. For the MZ3-S1400G specimen, the region with mullite-zirconia aggregates (see cyan dotted contours in Figure 12) exhibited flatter surfaces (Figure 12(a)) in comparison to sample MZ5-S1450G (Figure 12(b)). For example, the highlighted aggregate at the top of Figure 12(a) exhibited a predominantly dotted pattern, with dendrites from the eutectic structure being cut the same way along this surface. Conversely, no clear pattern is seen in the aggregate at the top region of Figure 12(b) since the dendritic structure appears to be cut along different planes. Similar comparisons can be made about the bigger aggregates in the middle of both fractographies and were consistently seen in other analyzed regions. Since no liquid phase or phase transformation was expected between 1400°C and 1450°C, the more tortuous crack path inside the eutectic aggregates was probably related to the strength of the interface between the aggregates and the matrix.

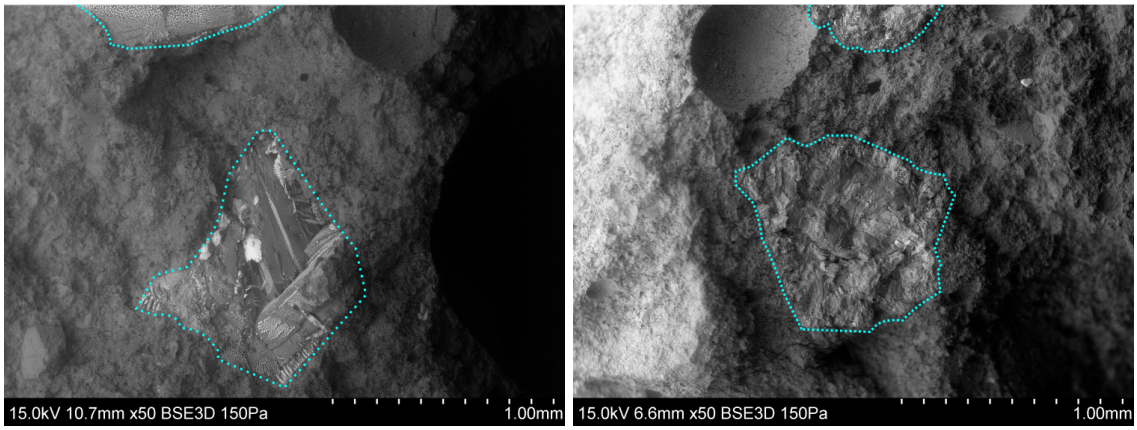

(a) (b)

Figure 12: SEM micrographs of fractured surfaces of samples MZ3-S1400G (a) and MZ5-S1450G (b). The cyan dotted lines highlight mullite-zirconia aggregates. Roughness differences indicate that the crack propagated along a more tortuous path for the latter, especially inside the mullite-zirconia aggregate.

5.4. Estimating the cohesive strength and fracture energy

The same experiments were first analyzed in Ref. [21], in which fracture energies estimations were reported. They are gathered in Table 6 where Γ_c^{raw} corresponds to the work performed by the testing machine (*i.e.,* calculated using the actuator displacement and vertical forces) divided by twice the projected fractured area. Since this measurement also considers the work to deform the testing machine and possibly other contributions such as friction, it provides an upper bound for the fracture energy. Conversely, Γ_c^{NOD} uses the work calculated with a very simple approximation of the horizontal load integrated with $1.62 \times NOD$ approximation of the CMOD. This estimate is likely to be a lower bound for the fracture energy since it does not account for the initiation energy [22]. Let us note that these preliminary calculations used the loading curve up to 10% of the ultimate load (post-peak), while in the present paper it was performed until 15%. Therefore, it was expected that the fracture energy J_c calibrated herein would lie between these two bounds,[1] which is observed to apply for the cases with grooves (*i.e.,* MZ1-S1450G, MZ3-S1400G, and MZ5-S1450G samples). The parameters c calibrated herein being lower than the initial value (1.62) indicates that the lower bound was even lower than that reported in Ref. [21], as suggested by Γ_c^{NOD-*} calculated with the new c values (Table 4). For the samples with no grooves (*i.e.,* MZ2-S1400 and MZ4-S1450) this estimation is not less than J_c, even if this is the case for the other three (grooved) cases. This difference may be explained by 3D effects that took place in the experiment, and were not fully accounted for by the plane strain hypothesis and reduced thickness in the groove.

[1] The factor two for their comparison comes from area considerations. Both Γ_c^{NOD} and Γ_c^{raw} consider *twice* the projected area since they are measures of the work necessary to create *two* new surfaces, while J_c considers the work to damage the intact plane in the material defined with the CZM

Moreover, Γ_c^{raw} showed to be an upper bound for all cases and could be used as a good initialization in the calibration procedure.

Table 6

Fracture energies calculated with different approaches for the five analyzed experiments. Γ_c^{NOD} and Γ_c^{NOD-*} were calculated with NOD data, Γ_c^{raw} with the actuator displacement, and J_c is the fracture energy for the calibrated CZM

Parameter	MZ1-S1450G	MZ2-S1400	MZ3-S1400G	MZ4-S1450	MZ5-S1450G
$2\times\Gamma_c^{NOD}$ [J/m^2] [♭]	212	382	306	454	410
$2\times\Gamma_c^{NOD-*}$ [J/m^2]	199	331	309	427	381
J_c [J/m^2]	266	327	361	405	456
$2\times\Gamma_c^{raw}$ [J/m^2] [♭]	286	454	374	528	508

[♭] after Ref. [21]

When the stress concentration at the pre-notch is not accounted for, and neglecting the flexural stresses caused by vertical forces, the so-called notch tensile strength $\sigma_{\max}$ was assessed from the sum of the tensile and flexural stresses at maximum load [13]

$$\sigma_{\max} = \frac{F_{H,\max}}{bh}\left(1+\frac{6y}{h}\right) \tag{6}$$

where $F_{H,\max}$ is the ultimate splitting (*i.e.,* horizontal) force, b the thickness and h the height of the ligament, and y the vertical distance from the loading point to the ligament center. Both quantities y and h refer to the reference configuration (*i.e.,* for an undamaged state). With the present geometry, the flexural contribution accounted for 85% of $\sigma_{\max}$, which is reported together with the calibrated cohesive strength σ_f in Table 7. As an initialization guideline, the present results indicate that a good estimation of σ_f consists in taking between 50% and 60% of $\sigma_{\max}$, as the latter can be easily calculated from the loading curve. If the flexural contribution alone was considered (*i.e.,* notch flexural strength), then a first order estimate was about 60% to 70% of $\sigma_{\max}^{flex}$. These observations are consistent with the fact that damage initiated when the applied force reached about 50% of the ultimate load (as discussed in the next section).

Table 7

Cohesive strength σ_f, notch tensile strength $\sigma_{\max}$, and their ratio calculated for the five analyzed experiments.

Parameter	MZ1-S1450G	MZ2-S1400	MZ3-S1400G	MZ4-S1450	MZ5-S1450G
σ_f [MPa]	4.3	3.5	3.9	3.7	3.8
$\sigma_{\max}$ [MPa]	7.3	6.3	7.2	6.6	7.5
$\sigma_f/\sigma_{\max}$ [%]	59	55	54	56	51
$\sigma_{\max}^{flex}$ [MPa]	6.2	5.3	6.1	5.6	6.3
$\sigma_f/\sigma_{\max}^{flex}$ [%]	69	66	64	66	60

5.5. Fracture Process Zone

In the present framework, the CZM parameters together with the Young's modulus allow for a direct calculation of the so-called Hillerborg length [6]

$$\ell_H = \frac{E J_c}{\sigma_f^2} \tag{7}$$

that can be used to estimate the Fracture Process Zone (FPZ) size [46, 47] and is reported in Table 8 for the five samples. The order of magnitude of the FPZ size is about one tenth of ℓ_H, which in this case is about the size of the ligament height. Therefore, it is expected that the FPZ developed throughout all the propagation region. Such effect was not discussed in Ref. [38] since the loading was stopped at 70% of the peak load. The length ℓ_H is influenced by the testing temperature, since all ℓ_H values calculated for 600°C tests were about twice that obtained for the room-temperature test. This difference is explained by different coefficients of thermal expansion of the matrix and aggregates that may cause further interlocks between crack faces, together with easier initiation of the weakened bonds at higher temperature. By increasing the sintering temperature by 50°C (*i.e.,* $\approx$ 3.5%), ℓ_H increased about 20%, when comparing samples MZ2-S1400 to MZ4-S1450, and MZ3-S1400G to MZ5-S1450G, which is related to a better consolidation of the alumina matrix and aggregate interfaces (see discussions of Figure 12). The presence of lateral grooves had less influence, *i.e.,* lower ℓ_H for the case sintered at 1400°C and higher for 1450°C, by similar amounts.

Table 8

Hillerborg length ℓ_H (Equation (7)) calculated for the five analyzed experiments

Parameter	MZ1-S1450G	MZ2-S1400	MZ3-S1400G	MZ4-S1450	MZ5-S1450G
ℓ_H [mm]	649	1201	1119	1378	1450

The space-time horizontal tractions in the cohesive elements are shown in Figure 13(a) for sample MZ1-S1450G. It corresponds to the mode I traction (σ_I) for a given element (rows) and time step (columns). The colored continuous lines show when the element started to be damaged (magenta) and when it achieved different levels of damage (*i.e.,* 20 and 90%, in red and green). To estimate the FPZ size for each time step, the number of damaged elements was counted (*i.e.,* between the magenta curve and the top of the spacetime images) and is shown in Figure 13(b). No element was fully damaged when using $\alpha = 7$ (this was not the case when $\alpha = 2$), which was also true in the following cases. This observation is consistent with the fact that the softening response extends over a wider range of separation for $\alpha = 7$ compared to $\alpha = 2$ (Figure 5). A numerical test case [48] showed that a bigger sample would be necessary for cases in which the ligament length was smaller than the expected FPZ size. It also corroborates the experimental observations, whereby after the test, most of the full ligament remained with very small openings. Last, let us note that damage initiated at $\approx$50% of the peak load (for $\alpha = 7$), which indicates that the BC corrections were performed for load levels

very close to damage initiation.

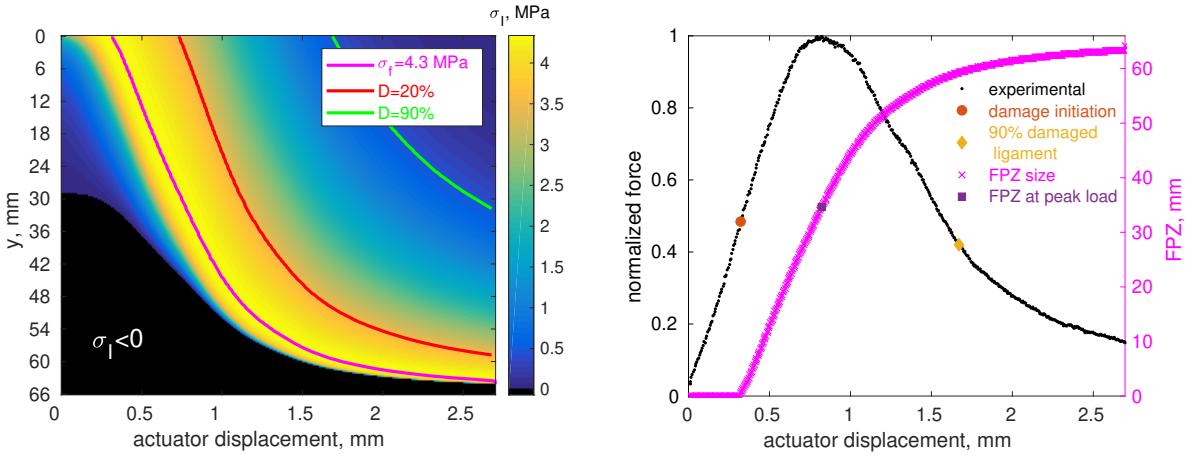

(a) (b)

Figure 13: (a) Space-time mode I tractions for the cohesive elements of sample MZ1-S1450G. Each row and column of the image represents one element and one time step, respectively. The full lines depict the initiation and propagation stages of damage. The black region indicates compressive stresses. (b) Normalized force and FPZ size measured by counting the number of damaged elements at given time step. The colored markers depict points of interest discussed in Table 9.

Three points of interest were selected for such curves, first exemplified in Figure 13(b) but shown below for all other samples, and are gathered in Table 9. Together with the forces for damage initiation (orange circle), Table 9 also reports the forces when 90% of the ligament length was damaged (yellow diamond), and the FPZ size for the ultimate load (purple square) for all experiments. The consistency of the results indicates that when such experiments are modeled as carried out herein, damage starts when the forces reach about half of the ultimate load. Moreover, in the present geometry in which the ligament was 66 mm long, damage was already present for more than half of its length at the peak load, and only a small part of the ligament was undamaged for approximately the same load levels in the softening part.

Table 9

Normalized force at damage initiation, and when 90% of the ligament length was damaged. FPZ size at the ultimate load

	MZ1-S1450G	MZ2-S1400	MZ3-S1400G	MZ4-S1450	MZ5-S1450G
normalized force at damage initiation	0.48	0.53	0.52	0.54	0.54
normalized force (post-peak) when 90% of the ligament was damaged	0.42	0.49	0.46	0.51	0.49
FPZ size at ultimate load (mm)	34.6	37.6	36.7	38.2	42.1

Similarly, the space-time mode I tractions and the FPZ estimates for the samples sintered at 1400°C (*i.e.,* MZ2-S1400 and MZ3-S1400G) are shown in Figure 14. Damage also initiated at ≈50% of the ultimate load, and the FPZ was already half developed at the ultimate load itself (*i.e.,*, there were damaged elements up to the half height of the ligament). Beyond this point, the FPZ development decelerated and saturated close to 30% of the ultimate load.

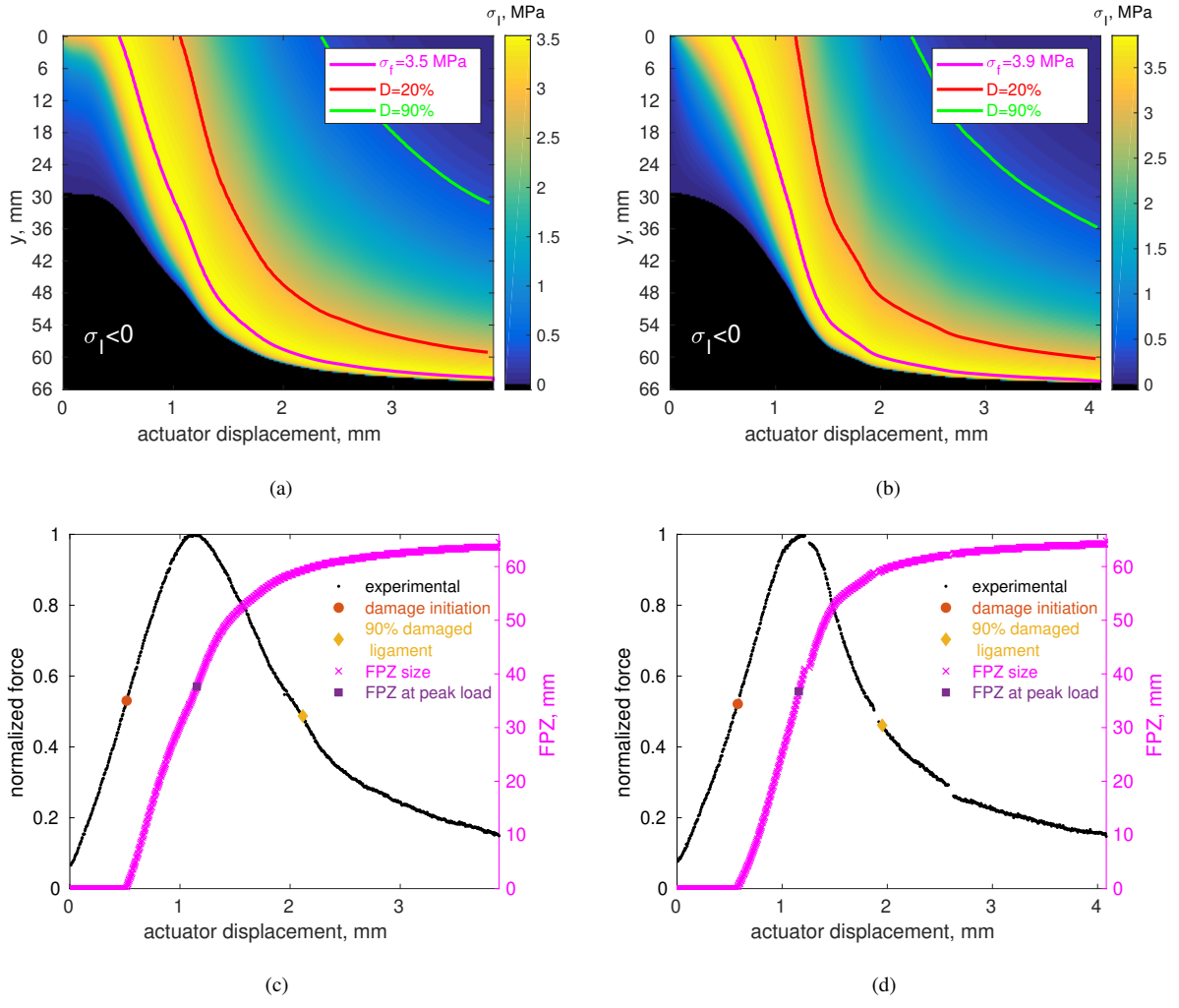

Figure 14: Space-time tractions for the cohesive elements of samples MZ2-S1400 (a) and MZ3-S1400G (b). Each row and column of the image represents one element and one time step, respectively. The full lines depict the initiation and propagation stages of damage. The black region indicates compressive stresses. Normalized force and FPZ size measured by counting the number of damaged elements at a given time step for samples MZ2-S1400 (c) and MZ3-S1400G (d). The colored markers depict points of interest reported in Table 9.

Analogous results are reported for MZ4-S1450 and MZ5-S1450G samples in Figure 15. The FPZ started to develop at 50% of the ultimate load and decelerated beyond the peak load. No element was fully damaged in any of the five analyzed cases, which was due to the long lower tail of the cohesive law (Figure 5). Last, the compressive region

became smaller as the cracks propagated, and remained quasi-constant for the last time steps.

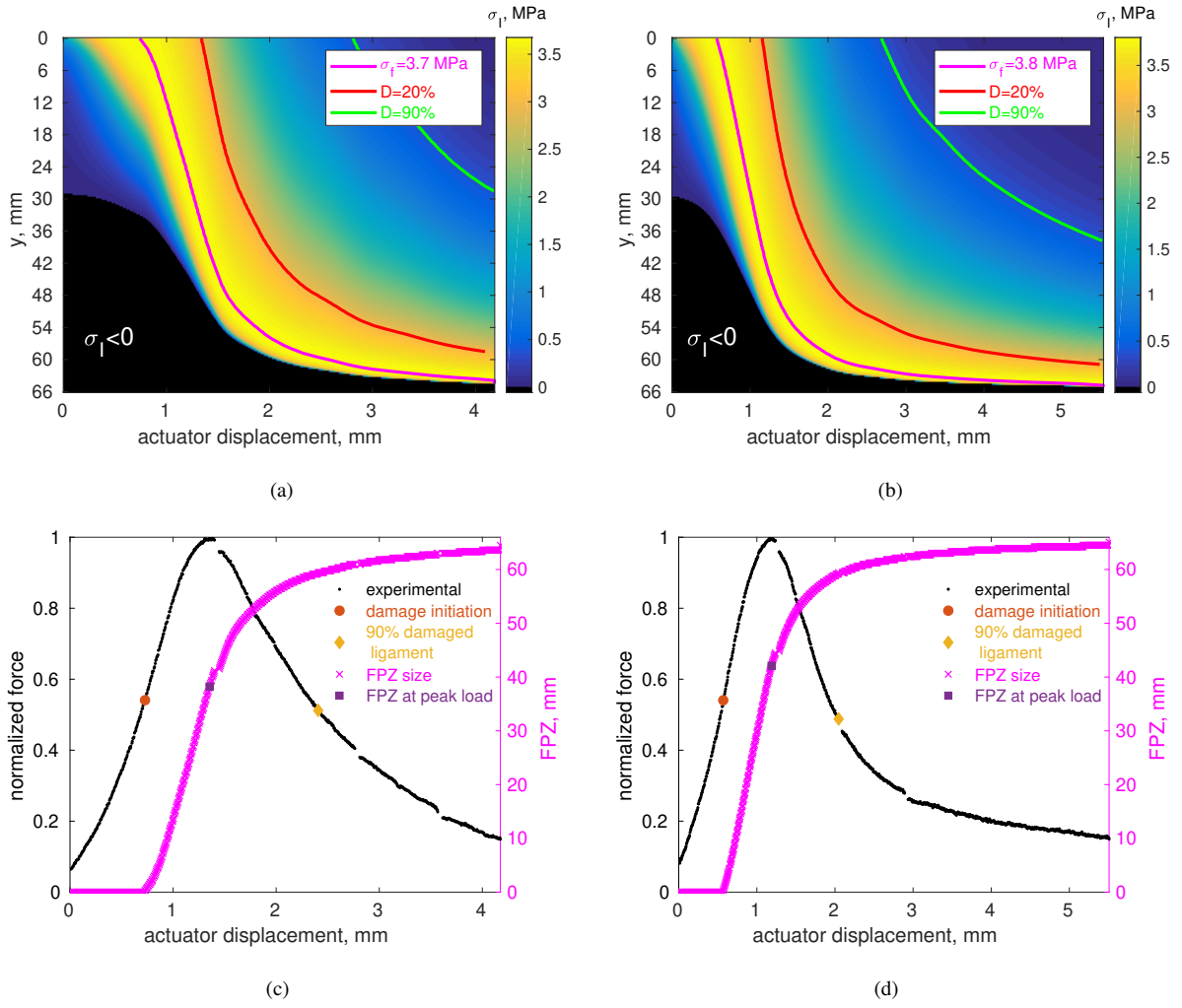

Figure 15: Space-time tractions for the cohesive elements of samples MZ4-S1450 (a) and MZ5-S1450G (b). Each row and column of the image represents one element and one time step, respectively. The full lines depict the initiation and propagation stages of damage. The black region indicates compressive stresses. Normalized force and FPZ size measured by counting the number of damaged elements at a given time step for samples MZ4-S1450 (c) and MZ5-S1450G (d). The colored markers depict points of interest discussed in Table 9.

6. Conclusion

Cohesive and boundary condition parameters were calibrated via weighted FEMU for an alumina-based castable refractory with mullite-zirconia aggregates from Wedge Splitting Tests (WSTs) performed at room-temperature and 600°C. The minimized cost-functions comprised the opening displacement in the notched region (NOD), measured via Digital Image Correlation (DIC) in the reduced field-of-view that was available, together with the applied forces.

Guidelines for the initialization of parameters in such procedures were also discussed.

The analysis of the shape parameter for the traction-separation law indicated that a bi-linear function ($\alpha = 2$) was less suitable for the studied material. It reinforced the fact that the fracture process zone extended through large regions even if only small cohesion remained between both cracked faces, since different toughening mechanisms may have been activated during crack propagation. The present study allowed the different sample treatments and testing conditions to be distinguished in terms of their effects on cohesive properties, and thus could be used for material selection purposes. For instance, even in experiments with very close ultimate loads, the cohesive strength was significantly different when the tests were performed at 600°C. General trends with respect to the measured forces were also highlighted such as damage initiating at half the ultimate load.

When the samples were sintered at a sightly higher temperature, the material cohesion was expected to be stronger, which reflected in a 10% higher cohesive strength. The increased cohesion between the different phases also induced a 20% increase in fracture energy, which may be interesting in different applications. SEM fractographies showed that an increase of 50°C led to a different crack propagation mechanism near the mullite-zirconia aggregates, namely, with increased roughness when traversing these aggregates. Moreover, higher sintering temperatures may also spread the fracture process zone, as suggested by increased Hillerborg lengths. Last, when two samples with the exact same treatment were tested at different temperatures, the one at 600°C showed a cohesive strength that was 10% smaller in conjunction with a 70% higher fracture energy, showing the importance of performing experiments as close as possible to in-service conditions.

One sample for each treatment was used to show the feasibility of such procedures. However, a study about the scatter of cohesive parameters is desirable. Such methods could also be applied at even higher temperatures and for different material compositions.

Acknowledgments

This study was financed in part by the Coordenação de Aperfeiçoamento de Pessoal de Nível Superior - Brasil (CAPES) - Finance Code 001 CAPES (Brazil) and #2018/15266-0, #2018/23081-0, #2020/08077-6, and #2021/09238-6 São Paulo Research Foundation (FAPESP), and by the French “Agence Nationale de la Recherche” through the “Investissements d’avenir” program (ANR-10-EQPX-37 MATMECA Grant). The authors would like to thank Prof. J.A. Rodrigues for fruitful discussions about WSTs, Mr. M. Bonnet for his help to acquire the SEM images, Mr. B. Smaniotto for the acquisition of the tomographic scans, and IBAR (Indústrias Brasileiras de Artigos Refratários, Poá, Brazil) for providing the studied material.

Credit authorship statement

R. Vargas: Conceptualization, Methodology, Investigation, Software, Original draft preparation, Writing - Review & Editing

R.B. Canto: Supervision, Conceptualization, Writing - Review & Editing, Resources, Funding acquisition, Project administration

F. Hild: Supervision, Conceptualization, Methodology, Software, Formal analysis, Writing - Review & Editing, Resources, Funding acquisition, Project administration

Declaration of Competing Interest

The authors declare that they have no known competing financial interests or personal relationships that could have appeared to influence the work reported in this paper.

References

[1] W. D. Callister, Ciência e Engenharia de Materiais: Uma Introdução Ed, 7th Edition, 2007.

[2] J. Poirier, E. Blond, E. Bilbao, R. Michel, A. Coulon, J. Gillibert, M. Boussuge, Y. Zhang, D. Ryckelynk, G. Dusserre, T. Cutard, P. Leplay, New advances in the laboratory characterization of refractories: testing and modelling, Metallurgical Research & Technology 114 (6) (2017) 610.

[3] W. E. Lee, W. Vieira, S. Zhang, K. Ghanbari Ahari, H. Sarpoolaky, C. Parr, Castable refractory concretes, International Materials Reviews 46 (3) (2001) 145–167.

[4] D. Dugdale, Yielding of steel sheets containing slits, J. Mech. Phys. Solids 8 (1960) 100–104.

[5] G. Barenblatt, The mathematical theory of equilibrium of crack in brittle fracture, Adv. Appl. Mech. 7 (1962) 55–129.

[6] A. Hillerborg, M. Modéer, P. E. Petersson, Analysis of crack formation and crack growth in concrete by means of fracture mechanics and finite elements, Cement and Concrete Research 6 (6) (1976) 773–782.

[7] M. Elices, G. Guinea, J. Gómez, J. Planas, The cohesive zone model: advantages, limitations and challenges, Engineering Fracture Mechanics 69 (2002) 137–163.

[8] K. Park, G. H. Paulino, J. R. Roesler, A unified potential-based cohesive model of mixed-mode fracture, Journal of the Mechanics and Physics of Solids 57 (6) (2009) 891–908.

[9] J.-D. Mathias, N. Tessier-Doyen, Homogenization of glass/alumina two-phase materials using a cohesive zone model, Computational materials science 43 (4) (2008) 1081–1085.

[10] I. Özdemir, W. A. M. Brekelmans, M. G. D. Geers, Modeling thermal shock damage in refractory materials via direct numerical simulation (DNS), Journal of the European Ceramic Society 30 (7) (2010) 1585–1597.

[11] J. Hein, O. El Khatib, M. Kuna, Influence of interfaces on crack propagation through a layered refractory loaded by thermal shock, JOURNAL OF CERAMIC SCIENCE AND TECHNOLOGY 7 (2) (2016) 203–208.

[12] A. Doitrand, R. Estevez, M. Thibault, P. Leplay, Fracture and cohesive parameter identification of refractories by Digital Image Correlation up to 1200 °C, Experimental Mechanics 60 (5) (2020) 577–590.

[13] H. Harmuth, K. Rieder, M. Krobath, E. Tschegg, Investigation of the nonlinear fracture behaviour of ordinary ceramic refractory materials, Materials Science and Engineering: A 214 (1-2) (1996) 53–61.

[14] H. Harmuth, E. K. Tschegg, A fracture mechanics approach for the development of refractory materials with reduced brittleness, Fatigue & Fracture of Engineering Materials & Structures 20 (11) (1997) 1585–1603.

[15] G. Buchebner, T. Molinari, D. Rumpf, Developing basic high-performance products for furnaces in the nonferrous metals industries, JOM 52 (2) (2000) 68–72.

[16] P.-Y. Brisson, E. Paransky, M. Rigaud, Effects of andalusite grain size on microstructure and mechanical properties of low cement alumina-based castables, Canadian metallurgical quarterly 42 (2) (2003) 157–165.

[17] E. Brochen, C. Dannert, P. Quirmbach, Thermo-mechanical characterisation of magnesia-carbon refractories by means of wedge splitting test under controlled atmosphere at high-temperature, in: Proceedings of the Unified International Technical Conference on Refractories (UNITECR 2013), Wiley Online Library, 2014, pp. 53–58.

[18] K. Andreev, V. Tadaion, Q. Zhu, W. Wang, Y. Yin, T. Tonnesen, Thermal and mechanical cyclic tests and fracture mechanics parameters as indicators of thermal shock resistance–case study on silica refractories, Journal of the European Ceramic Society 39 (4) (2019) 1650–1659.

[19] S. Jin, H. Harmuth, Asymmetric creep modeling of common refractory ceramics with high temperature wedge splitting test, Engineering Fracture Mechanics 252 (2021) 107819.

[20] S. Samadi, S. Jin, H. Harmuth, Combined damaged elasticity and creep modeling of ceramics with wedge splitting tests, Ceramics International 47 (18) (2021) 25846–25853.

[21] R. Vargas, X. Pinelli, B. Smaniotto, F. Hild, R. B. Canto, On the effect of sintering temperature on fracture energy of Alumina-Mullite-Zirconia castable at 600°C, Journal of the European Ceramics Society 41 (7) (2021) 4406–4418.

[22] R. Vargas, R. B. Canto, F. Hild, Fracture energy evaluation of refractories in wedge splitting tests from notch opening displacements, Journal of the European Ceramic Society 41 (10) (2021) 5367–5379.

[23] R. Vargas, R. Canto, F. Hild, On the calibration of cohesive parameters for refractories from notch opening displacements in wedge splitting tests, Journal of the European Ceramic Society 41 (14) (2021) 7348–7361.

[24] E. C. Subbarao, H. S. Maiti, K. K. Srivastava, Martensitic transformation in zirconia, Physica status solidi (a) 21 (1) (1974) 9–40.

[25] R. C. Garvie, R. H. Hannink, R. T. Pascoe, Ceramic steel?, Nature 258 (5537) (1975) 703–704.

[26] R. H. J. Hannink, P. M. Kelly, B. C. Muddle, Transformation toughening in zirconia-containing ceramics, Journal of the American Ceramic Society 83 (3) (2000) 461–487.

[27] C. Jailin, A. Bouterf, R. Vargas, F. Hild, S. Roux, Sub-minute In Situ Fracture Test in a Laboratory CT Scanner, Integrating Materials and Manufacturing Innovation 8 (3) (2019) 413–422.

[28] S. Ribeiro, C. C. D. Exposito, J. A. Rodrigues, Projeto, adaptação, instalação e testes preliminares para um sistema de medida de energia de fratura de materiais cerâmicos pelo método da cunha, Cerâmica 54 (2008) 418–426.

[29] M. C. Greca, J. V. Emiliano, A. M. Segadães, Revised phase equilibrium relationships in the system Al_2O_3-ZrO_2-SiO_2, Journal of the European Ceramic Society 9 (4) (1992) 271–283.

[30] V. R. Salvini, V. C. Pandolfelli, R. C. Bradt, Extension of hasselman's thermal shock theory for crack/microstructure interactions in refractories, Ceramics International 38 (7) (2012) 5369–5375.

[31] D. Y. Miyaji, T. Tonnesen, J. A. Rodrigues, Fracture energy and thermal shock damage resistance of refractory castables containing eutectic aggregates, Ceramics International 40 (9, Part B) (2014) 15227–15239.

[32] R. Vargas, R. B. Canto, F. Hild, S. Roux, On accounting for speckle extinction via DIC and PCA, Optics and Lasers in Engineering 149 (2022)

106813.

[33] J. Lyons, J. Liu, M. Sutton, High-temperature deformation measurements using digital-image correlation, Exp. Mech. 36 (1) (1996) 64–70.

[34] K. Kavanagh, R. Clough, Finite element applications in the characterization of elastic solids, Int. J. Solids Struct. 7 (1971) 11–23.

[35] K. Kavanagh, Extension of classical experimental techniques for characterizing composite-material behavior, Exp. Mech. 12 (1) (1972) 50–56.

[36] E. Pagnacco, A.-S. Caro-Bretelle, P. Ienny, Parameter Identification from Mechanical Field Measurements using Finite Element Model Updating Strategies, Wiley-Blackwell, 2012, Ch. 9, pp. 247–274.

[37] K. Park, G. H. Paulino, Computational implementation of the PPR potential-based cohesive model in ABAQUS: educational perspective, Engineering Fracture Mechanics 93 (2012) 239–262.

[38] R. Vargas, J. Neggers, R. B. Canto, J. A. Rodrigues, F. Hild, Analysis of a castable refractory using the wedge splitting test and cohesive zone model, Journal of the European Ceramic Society 39 (13) (2019) 3903–3914.

[39] P. R. Lipow, I. J. Schoenberg, Cardinal interpolation and spline functions. III. Cardinal Hermite interpolation, Linear Algebra and its Applications 6 (1973) 273–304.

[40] S. Roux, F. Hild, Optimal procedure for the identication of constitutive parameters from experimentally measured displacement fields, International Journal of Solids and Structures 184 (2020) 14–23.

[41] R. Vargas, A. Tsitova, F. Bernachi-Barbe, B. Bary, R. B. Canto, F. Hild, On the identification of cohesive zone model for curved crack in mortar, Strain 56 (6) (2020) e12364.

[42] F. Hild, S. Roux, Digital image correlation, in: P. Rastogi, E. Hack (Eds.), Optical Methods for Solid Mechanics. A Full-Field Approach, Wiley-VCH, Weinheim (Germany), 2012, pp. 183–228.

[43] R. Vargas, J. Neggers, R. B. Canto, J. A. Rodrigues, F. Hild, Comparison of two full-field identification methods for the wedge splitting test on a refractory, Journal of the European Ceramic Society 38 (16) (2018) 5569 – 5579.

[44] C. R. Ferrari, J. A. Rodrigues, Microstructural features of alumina refractories with mullite-zirconia aggregates, Boletin-Sociedad Española de Ceramica y Vidrio 42 (1) (2003) 15–20.

[45] F. H. Wittmann, V. Slowik, A. M. Alvaredo, Probabilistic aspects of fracture energy of concrete, Materials and Structures 27 (9) (1994) 499–504.

[46] L. Saucedo, C. Y. Rena, G. Ruiz, Fully-developed FPZ length in quasi-brittle materials, International Journal of Fracture 178 (1-2) (2012) 97–112.

[47] W. Dong, X. Zhou, Z. Wu, On fracture process zone and crack extension resistance of concrete based on initial fracture toughness, Construction and Building Materials 49 (2013) 352–363.

[48] R. Vargas, F. Hild, R. B. Canto, Defining specimen size for the wedge splitting test to analyze the fracture process zone, in: 5th Brazilian Conference on Composite Materials (BCCM5), São Carlos, Brazil (online), 2021.

Appendix A: Sensitivity analyses

The sensitivities for both F_{FE} and $\mathrm{NOD}_{\mathrm{FE}}$ (*i.e.,* their partial derivatives with respect to the sought parameters $\{\mathbf{p}\}$) were calculated via finite differences with a 1% perturbation of each current estimate of the parameters, $\{\mathbf{p_n}\}$. They will be called $[\mathbf{S}_F]$ and $[\mathbf{S}_{\mathrm{NOD}}]$. These sensitivities allowed the dimensionless Hessian $[\mathbf{H}]$ to be calculated

$$[\mathbf{H}] = \frac{1}{\gamma_{\mathrm{F}}^2}\left[\mathbf{S}_F\right]^\top\left[\mathbf{S}_F\right] + \frac{1}{\gamma_{\mathrm{NOD}}^2}\left[\mathbf{S}_{\mathrm{NOD}}\right]^\top\left[\mathbf{S}_{\mathrm{NOD}}\right] \tag{8}$$

The minimization procedure was then performed by iteratively updating the current estimate of parameters by solving linear systems

$$[\mathbf{H}]\cdot\{\delta\mathbf{p}\} = \{\mathbf{h}\} \tag{9}$$

where the right hand member $\{\mathbf{h}\}$ reads

$$\{\mathbf{h}\} = \frac{1}{\gamma_{\mathrm{F}}^2}\left[\mathbf{S}_F\right]^\top\left\{R_F(t,\{\mathbf{p}_n\})\right\} + \frac{1}{\gamma_{\mathrm{NOD}}^2}\left[\mathbf{S}_{\mathrm{NOD}}\right]^\top\left\{R_{NOD}(t,\{\mathbf{p}_n\})\right\} \tag{10}$$

with R_F and R_{NOD} the difference between measured quantities and their simulated counterparts for the current parameter estimate. The iterative procedure stopped when the root mean square of the relative corrections $\{\delta\mathbf{p}\}$ was less than 10^{-2}. Last, the square root of the diagonal of the covariance matrix (*i.e.,* the inverse of $[\mathbf{H}]$) expresses the uncertainty fraction related to the standard deviation for each parameter when considered individually. It is reported in Tables 4, 5, and 11.

Although it was shown that performing such identification was possible with very few (*i.e.,* twelve) images (or time steps) [23], the condition number of the Hessian matrices reported in Table 10 highlights the fact that the more images are available, the lower the condition number and the easier the calibration of the sought parameters, which is especially important when analyzing high-temperature experiments for which higher NOD uncertainties were observed (Table 2).

Table 10

Number of images and condition number of the Hessian matrix for each analyzed experiment

	MZ1-S1450G	MZ2-S1400	MZ3-S1400G	MZ4-S1450	MZ5-S1450G
Image number	486	702	714	730	970
Condition number	92	29	17	23	11

For the sake of illustration, the sensitivities S_F, S_{NOD}, and the global Hessian matrices $[\mathbf{H}]$ are reported for the calibrated parameters (Table 5) in Figures 16-20 for each analyzed test. For sample MZ1-S1450G, corresponding to the only test performed at room temperature, each parameter affects differently the sensitivities S_F (Figure 16(a)) and

S_{NOD} (Figure 16(b)) during the loading history. For instance, the BCc parameter correcting for the load offset at the reference state is the only parameter significantly influencing the forces at the very beginning, as expected, while the fracture energy is more influential at the end when many elements were damaged (for both force and NOD data). Moreover, the NOD is not very sensitive at the first time steps for all parameters (*i.e.,* when the openings were small). For the last loading steps, the NOD sensitivity is dominated by the parameter c (it remained linear out of the range shown in the plot), which also leads to the highest value in the Hessian matrix (Figure 16(c)). It is worth noting that the eigen values of the Hessian matrix span over less than two orders of magnitude (Table 10), which make the identification procedure very robust for all considered parameters.

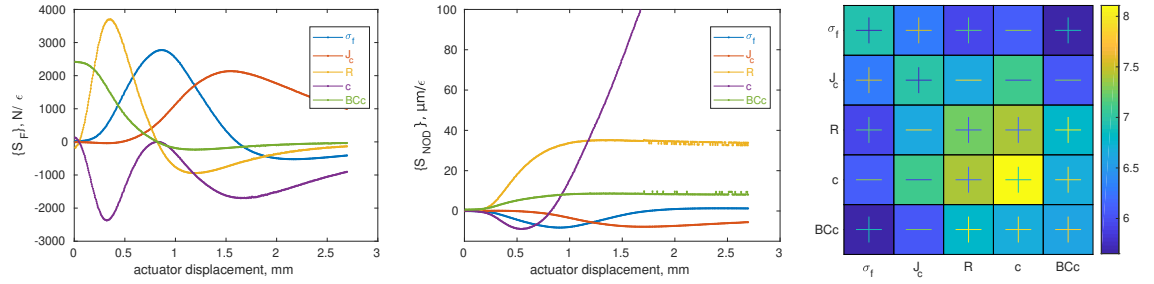

(a) (b) (c)

Figure 16: Sensitivities in force (S_F) (a) and NOD (S_{NOD}) (b). (c) Absolute Hessian matrix [$\mathbf{H}$] expressed in decimal logarithm for sample MZ1-S1450G.

For sample MZ2-S1400, the high value of the BCc parameter (*i.e.,* $BCc = 2.191$) changes how R and c affect the forces (Figure 17(a)) at the very beginning of the test when compared to the previous case (Figure 16(a)). This point highlights the nonlinear relationship between parameters. Even some influence is seen for small load levels in the NOD sensitivities (Figure 17(b)). The eigen values of the Hessian matrix shown in Figure 17(c) span slightly over one order of magnitude (*i.e.,* better condition number when compared to the previous case). This trend is believed to be caused by having 40% more images (*i.e.,* 702 against 486). The condition number for this case is the highest among all 600°C experiments (Table 10).

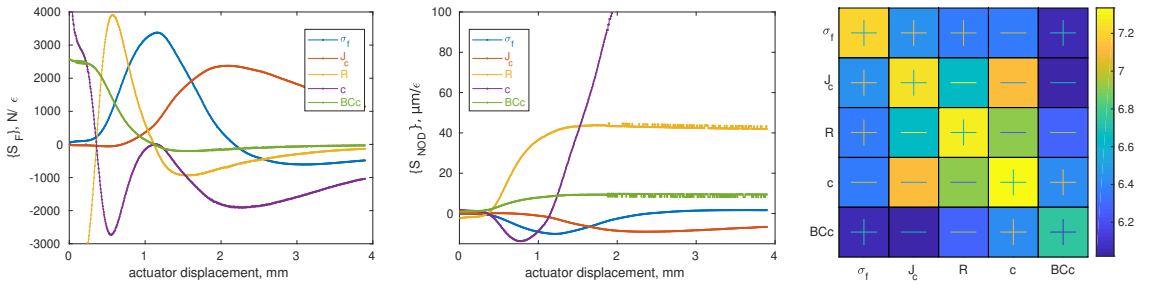

(a) (b) (c)

Figure 17: Sensitivities in force (S_F) (a) and NOD (S_{NOD}) (b). (c) Absolute Hessian matrix [**H**] expressed in decimal logarithm for sample MZ2-S1400.

One key aspect that is true for all cases studied herein is that the force and NOD sensitivities have very different temporal changes. For instance, for sample MZ3-S1400G, the parameters $\boldsymbol{R}$ and $\boldsymbol{BCc}$ have very close influences in terms of NOD sensitivities (Figure 18(b)), namely, they are essentially proportional to each other with a factor approximately equal to 4. Consequently, if only NOD data were considered, the minimization scheme would encounter multiple local minima. However, when the force sensitivities $\boldsymbol{S_F}$ are analyzed for the same parameters (Figure 18(a)), it is observed that their temporal changes are uncoupled for the first part of the test. As the condition number of the corresponding Hessian matrix (Figure 18(c)) was rather low (Table 10), it shows that both parameters could be calibrated with a similar uncertainty level thanks to the fact that two independent sets of data were utilized in the calibration procedure.

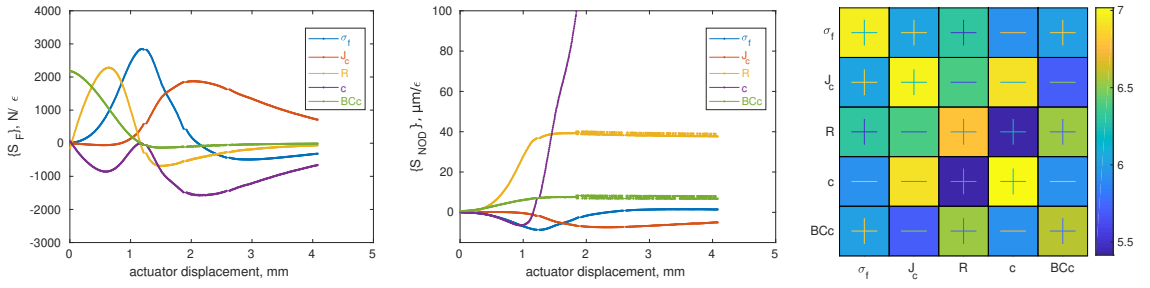

(a) (b) (c)

Figure 18: Sensitivities in force (S_F) (a) and NOD (S_{NOD}) (b). (c) Absolute Hessian matrix [**H**] expressed in decimal logarithm for sample MZ3-S1400G.

The overall trends seen for sample MZ4-S1450 are qualitatively close to the previous cases. It is interesting to note that the sensitivities related to the cohesive strength σ_f start from zero, increase up to a maximum around the ultimate load before decreasing at the end of the test (Figure 19). This fact is explained by the elements being undamaged at the beginning and most of the initiation phase occurs around the ultimate load. Checking the off-diagonal terms in the

Hessian matrix (Figure 19(c)), a high negative correlation is observed between J_c and c, which can also be inferred when their load sensitivities S_F are compared from 1.5 mm of actuator displacement to the end (*i.e.,* they are almost symmetric with respect to the horizontal axis).

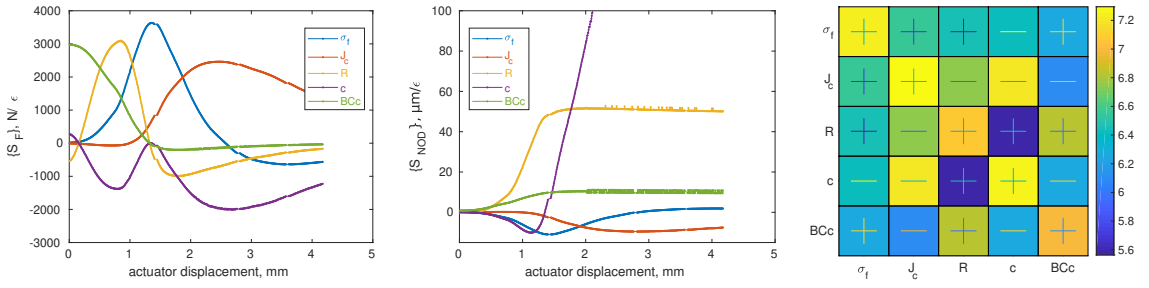

(a) (b) (c)

Figure 19: Sensitivities in force (S_F) (a) and NOD (S_{NOD}) (b). (c) Absolute Hessian matrix [**H**] expressed in decimal logarithm for sample MZ4-S1450.

Last, the results for sample MZ5-S1450G are presented in Figure 20. The relatively high BCc parameter has intermediate influences on the parameters c and R for the load sensitivity S_F (Figure 20(a)). Small fluctuations are observed in the NOD sensitivities S_{NOD} (Figure 20(b)) for parameters R and BCc, which are related to numerical oscillations due to very high levels of damage in many cohesive elements. The Hessian matrix (Figure 20(c)) has eigen values spanning over only one order of magnitude. The best condition number of this whole study (Table 10) is believed to be due to a finer discretization in time (*i.e.,* test with highest number of acquired images). Since the overall actuator displacement was the largest among all studied experiments, the parameter c and its influence in the NOD sensitivity S_{NOD} became even more dominant in the Hessian matrix (Figure 20(c)).

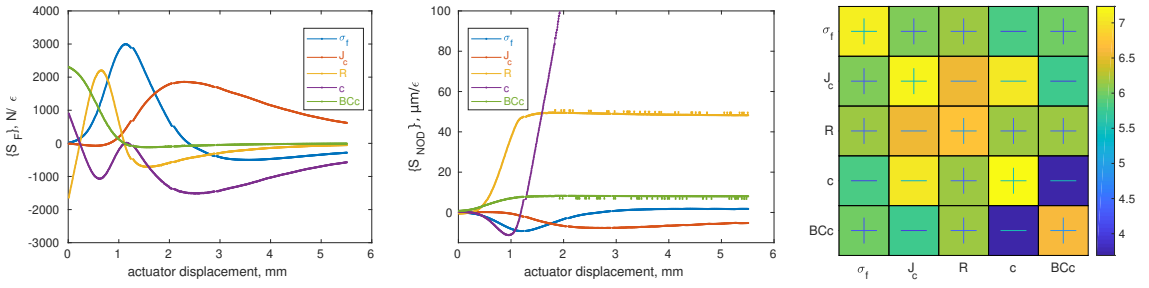

(a) (b) (c)

Figure 20: Sensitivities in force (S_F) (a) and NOD (S_{NOD}) (b). (c) Absolute Hessian matrix [**H**] expressed in decimal logarithm for sample MZ5-S1450G.

Appendix B: Identification results when $\alpha = 2$

All the parameters calibrated when using $\alpha = 2$ (*i.e.,* a bi-linear traction separation law, see Figure 5) together with their standard uncertainty (calculated from the covariance matrix as explained in Appendix A) are reported in Table 11. Overall, the discussion for $\alpha = 7$ (Sections 5.2 and 5.3) is also appropriate for this case. Considering the same experiment, by changing only α from 2 to 7 in the identification framework, the cohesive strength σ_f increased by about 10%, the fracture energy J_c by 5%, R decreased and BCc increased by smaller amounts (apart from a small decrease for sample MZ2-1400) than the CZM parameters. The parameter c showed smaller deviations, increasing in both grooved cases and decreasing for the others.

Table 11

Converged parameter sets for identifications using $\alpha = 2$ with respective standard uncertainties ($\pm$)

Parameter	MZ1-S1450G	MZ2-S1400	MZ3-S1400G	MZ4-S1450	MZ5-S1450G
σ_f [MPa]	3.960 ± 0.001	3.225 ± 0.0008	3.531 ± 0.001	3.321 ± 0.0008	3.523 ± 0.0009
J_c [J/m^2]	249.3 ± 0.08	315.6 ± 0.2	337.9 ± 0.2	383.4 ± 0.2	421.9 ± 0.2
R	2.339 ± 0.0009	2.492 ± 0.001	1.495 ± 0.001	1.679 ± 0.0008	1.761 ± 0.0009
c	1.4400 ± 0.0002	1.440 ± 0.0008	1.599 ± 0.0009	1.530 ± 0.0008	1.492 ± 0.0005
BCc	1.180 ± 0.0009	2.285 ± 0.001	1.034 ± 0.0008	1.189 ± 0.0005	1.671 ± 0.0009